iScience

CellPress
OPEN ACCESS

Article

# Altered synaptic plasticity of the longitudinal dentate gyrus network in noise-induced anxiety

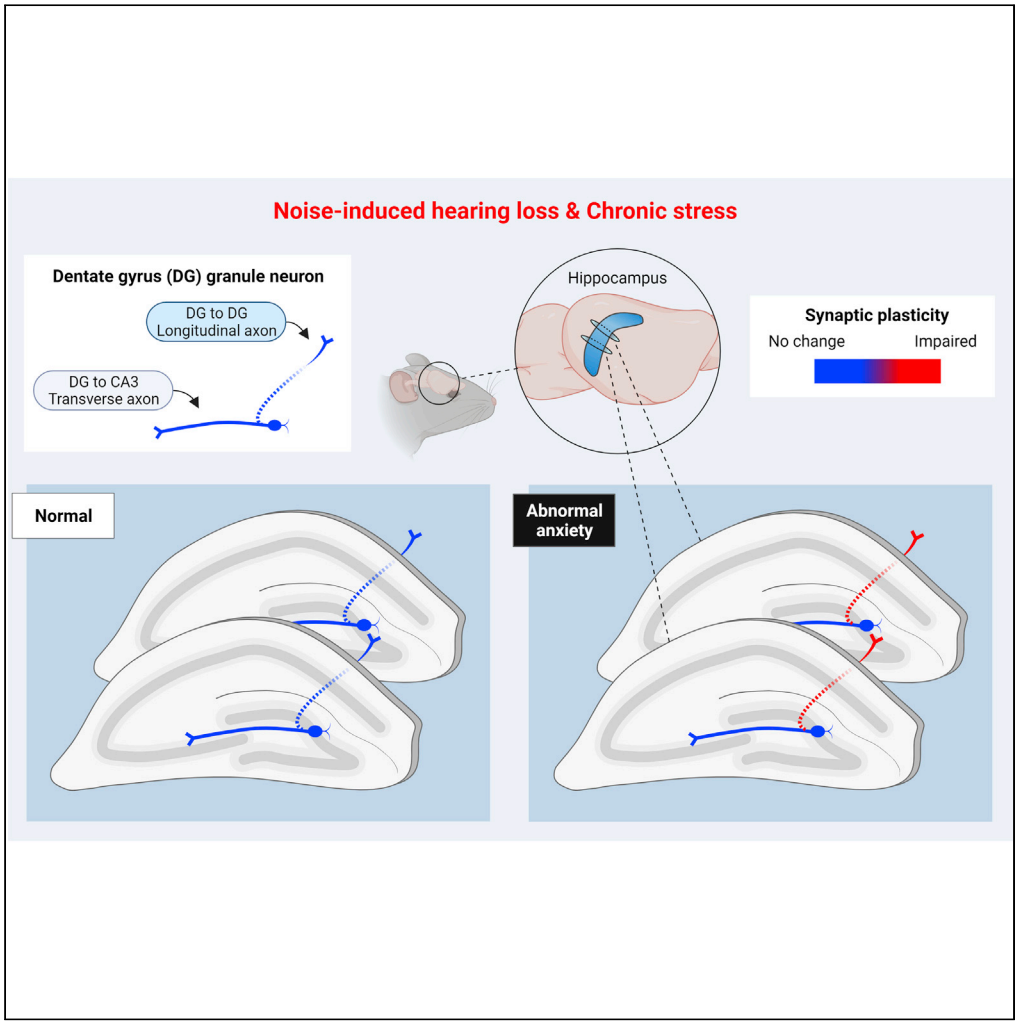


Sojeong Pak, Gona Choi, Jaydeep Roy, ..., Shaowen Bao, Sunggu Yang, Sungchil Yang

rebecpak2@gmail.com (S.P.)
abiyang9@gmail.com (S.Y.)
sungchil.yang@cityu.edu.hk (S.Y.)

## Highlights

Traumatic noise-induced hearing loss enhances anxiety-like behaviors

The longitudinal DG-DG network displays robust synaptic efficacy and plasticity

Abnormal anxiety is associated with synaptic alterations of the DG-DG network

DG-related brain disorders might stem from dysfunctional DG-DG networks

Pak et al., iScience 25, 104364
June 17, 2022 
https://doi.org/10.1016/j.isci.2022.104364

iScience

CellPress
OPEN ACCESS

Article

# Altered synaptic plasticity of the longitudinal dentate gyrus network in noise-induced anxiety

Sojeong Pak,[1,5,*] Gona Choi,[1,5] Jaydeep Roy,[2] Chi Him Poon,[2] Jinho Lee,[3] Dajin Cho,[1] Minseok Lee,[1] Lee Wei Lim,[2] Shaowen Bao,[4] Sunggu Yang,[3,*] and Sungchil Yang[1,6,*]

## SUMMARY

**Anxiety is characteristic comorbidity of noise-induced hearing loss (NIHL), which causes physiological changes within the dentate gyrus (DG), a subfield of the hippocampus that modulates anxiety. However, which DG circuit underlies hearing loss-induced anxiety remains unknown. We utilize an NIHL mouse model to investigate short- and long-term synaptic plasticity in DG networks. The recently discovered longitudinal DG-DG network is a collateral of DG neurons synaptically connected with neighboring DG neurons and displays robust synaptic efficacy and plasticity. Furthermore, animals with NIHL demonstrate increased anxiety-like behaviors similar to a response to chronic restraint stress. These behaviors are concurrent with enhanced synaptic responsiveness and suppressed short- and long-term synaptic plasticity in the longitudinal DG-DG network but not in the transverse DG-CA3 connection. These findings suggest that DG-related anxiety is typified by synaptic alteration in the longitudinal DG-DG network.**

## INTRODUCTION

Hearing loss is a common affliction in modern society and occurs in over 5% of the world's population (430 million). It is often caused by exposure to loud noises during daily activities such as work and recreation. The prevalence of hearing loss is expected to increase to 700 million people in the next 30 years, in turn increasing the related economic burden and depreciating the quality of life (Nelson et al., 2005). Noise-induced hearing loss (NIHL) can develop into hearing disorders, such as tinnitus, hyperacusis, and sensory overload. It can predispose individuals to psychiatric disorders, such as cognitive decline, dementia, depression, anxiety, and psychoses (Bhatt et al., 2017; Deal et al., 2017; Blazer and Tucci, 2019; Yang and Bao, 2013).

The dentate gyrus (DG) is a hippocampal subfield that modulates anxiety levels in response to environmental stresses. Neurogenesis and the neuronal activity of DG granule cells (DGGCs), the principal neurons in the DG, are closely correlated with stress-induced anxiety (Anacker et al., 2018; Hill et al., 2015; Kheirbek et al., 2013; Koch et al., 2020; Weeden et al., 2015). In particular, NIHL is associated with increased anxiety and impaired social interaction (Guitton, 2009; Lauer et al., 2018; Zheng et al., 2011). DG has an immense influence on these types of behaviors (Kheirbek et al., 2013; Leung et al., 2018; Zou et al., 2016). Indeed, hearing loss induces oxidative stress, tau phosphorylation, aberrant neurotransmitter receptor expression, and impaired neurogenesis and decreases the dendritic complexity of DGGCs (Nadhimi and Llano, 2021). However, it is unknown how the DG transmits incoming signals to neural networks to affect cognition subsequent to hearing loss.

The DG is an initial processing region in the cortico-hippocampal network that receives information from the second layer of the entorhinal cortex (EC) (ECII-DG-CA3 or CA2-CA1-subiculum) (Blaabjerg and Zimmer, 2007). The DG has three distinct layers: molecular, granule cell, and polymorphic (including the adult-born granule cell layer and the dentate hilus) (Amaral et al., 2007). The molecular layer is cell-sparse and mostly comprises dendrites of DGGCs. It is divided into three parts: inner, middle, and outer. The somata of granule cells are densely packed within the granule cell layer. Neurons in the molecular and granule cell layers receive inputs from the EC and dentate hilus and then send signals to the dentate hilus and CA3 and CA2 regions, respectively (Kohara et al., 2014; Blaabjerg and Zimmer, 2007; Swanson et al., 1978). In our previous study, we found that primary axons from the DG project transversely (in-lamellar) to the hilus and/or CA3 and bifurcate longitudinally (trans-lamellar) towards the molecular layer,

[1]Department of Neuroscience, City University of Hong Kong, 83 Tat Chee Avenue, Kowloon, Hong Kong SAR, China

[2]School of Biomedical Sciences, Li Ka Shing Faculty of Medicine, The University of Hong Kong, Hong Kong SAR, China

[3]Department of Nano-Bioengineering, Incheon National University, Incheon 22012, South Korea

[4]Department of Physiology, University of Arizona, Tucson, AZ 85724, USA

[5]These authors contributed equally

[6]Lead contact

*Correspondence: rebecpak2@gmail.com (S.P.), abiyang9@gmail.com (S.Y.), sungchil.yang@cityu.edu.hk (S.Y.)

https://doi.org/10.1016/j.isci.2022.104364

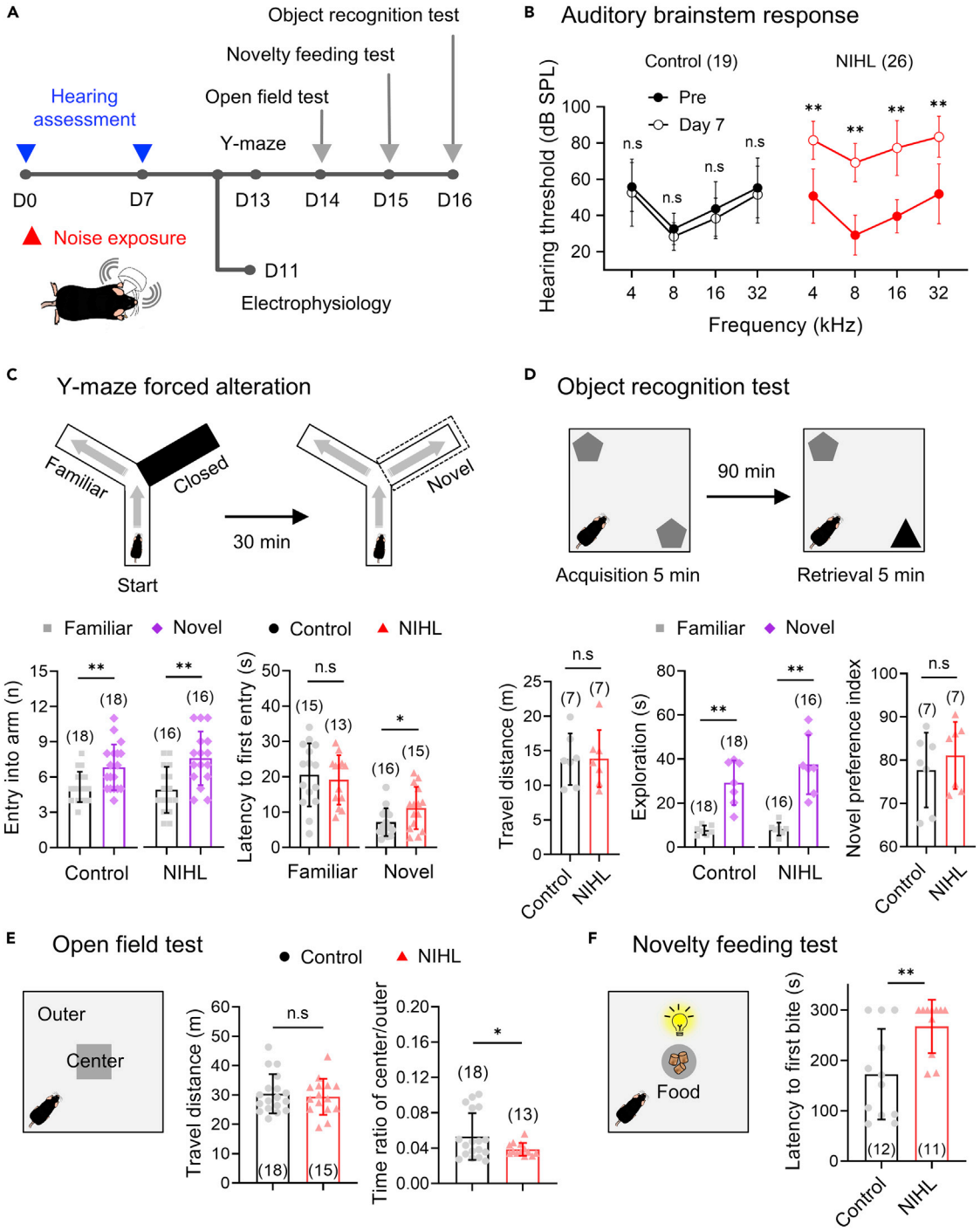


**Figure 1. NIHL enhances anxious behaviors**

(A) Timeline of the experimental procedure.

(B) Hearing threshold (dB sound pressure level [SPL]) at different frequency tones, as measured by the auditory brainstem response (ABR) recorded during pre- and post-noise (D7) exposure. Noise exposure elevates the hearing threshold.

(C) The total number of entries and the latency to the first entry into each arm in the Y-maze forced alteration task. NIHL significantly increases the latency to the first entry to the novel arm.

(D) The total distance traveled in an open field arena and the exploration time with the novel or familiar object during object recognition. Both the control and NIHL have novel object preference over familiar one.

**Figure 1. *Continued***

(E) The total area moved and the time (s) ratio of the center zone to the outer zone in the open field test. The ratio is reduced in NIHL. Individual data points have been eliminated for clearer visibility.

(F) The latency to the first food bite in the novelty-suppressed feeding test. In NIHL, the latency to food biting is increased. The numbers in parentheses indicate the number of animals tested.

Data are presented as means ± SD. NIHL: noise-induced hearing loss; *p < 0.05; **p < 0.01; n.s.: not significant. Also, see Table S1.

targeting adjacent DGGCs (Choi et al., 2021). This creates diverse DG axonal projection patterns that contain granule and mossy cells (Lømo, 2009; Claiborne et al., 1986; Scharfman and Pierce, 2012; Jonas and Lisman, 2014; Choi et al., 2021), as further evidenced by the longitudinal spread of electrical signals along the dorsoventral axis of the hippocampus (Pare and Llinas, 1994; Lømo, 2009). Like CA1-CA1 longitudinal axons, DG-DG longitudinal axons show more varicosities and smaller axon widths than DG-CA3 transverse axons (Choi et al., 2021; Yang et al., 2014a).

This study aimed to investigate the effects of NIHL on the DG network along two directions: the transverse DG-CA3 and the longitudinal DG-DG projections. We found that mice that experienced NIHL displayed abnormal anxiety-like behaviors, which was associated with altered synaptic properties in the DG-DG network but not in the DG-CA3 network. Furthermore, in a chronic stress-induced anxiety animal model, we observed alterations of the short- and long-term synaptic properties of the DG-DG network, similar to the effects of NIHL. Our findings suggest that alterations of the DG-DG network, but not of the DG-CA3 network, can predict anxiety-like behaviors.

## RESULTS

### NIHL enhances anxious behaviors

Unilateral hearing loss caused by exposure to loud noise was chosen to minimize the disruption of hearing-dependent normal behaviors. First, the auditory brainstem response (ABR) was recorded to check hearing ability before and after noise exposure (Figure 1A). The NIHL C57BL/6J mice showed elevated hearing thresholds in the noise-exposed ears in response to tones at each testing frequency (4 kHz, 8 kHz, 16 kHz, and 32 kHz) at 7 days after noise exposure (repeated-measures two-way ANOVA, pre vs. day 7, $F(1,50) = 196.979$, $p < 0.0001$). Unlike the NIHLs, the sham control mice (under anesthesia with no noise trauma) showed no threshold shifts (repeated-measures two-way ANOVA, pre vs. day 7, $F(1,36) = 1.32$, $p = 0.285$, see Table S1 for detail) (Figure 1B). These results indicate that our NIHL animal model experienced a severe degree of hearing loss.

Next, we examined whether hearing loss impairs spatial memory, as has been previously reported (Manohar et al., 2020; Liu et al., 2018). In the Y-maze forced alteration task, NIHL mice retained the novel arm preference over the familiar arm similar to control mice (control entries: familiar, 5.17 ± 1.29 times, n = 18 vs. novel, 6.83 ± 1.95 times, n = 18, paired *t* test, $t(17) = -3.18$, $p = 0.005$; NIHL entries: familiar, 4.88 ± 1.96 times, n = 16 vs. novel, 7.56 ± 2.28 times, n = 16, paired *t* test, $t(15) = -3.63$, $p = 0.002$). This result indicates no short-term spatial memory impairment in our NIHL model (Figure 1C). The lack of close involvement of NIHL with short-term memory was supported by the results of the object recognition test, which is commonly used to assess the behavioral aspects of recognition memory (Figure 1D). Although the total distance traveled (control, 13.77 ± 3.71 m, n = 7 vs. NIHL, 13.86 ± 4.14 m, n = 7, one-way ANOVA, $F(1,12) = 0.002$, $p = 0.968$) was not significantly different between the control and NIHL groups, both groups showed significantly higher exploration time on a novel object than that on a familiar object (control: familiar, 7.69 ± 2.12 s, n = 7 vs. novel, 29.21 ± 10.12 s, n = 7, paired *t* test, $t(6) = 5.433$, $p = 0.002$, NIHL: familiar, 8.13 ± 2.90 s, n = 7 vs. novel, 37.36 ± 13.43 s, n = 7, paired *t* test, $t(6) = 5.724$, $p = 0.001$) with no significant difference on novel object preference index between them (control, 77.71 ± 8.67%, n = 7 vs. NIHL, 81.07 ± 7.74%, n = 7, one-way ANOVA, $F(1,12) = 0.585$, $p = 0.459$) which implies no prominent impairments of recognition memory by NIHL.

However, as in the Figure 1C, the NIHLs significantly increased the latency to the first entry into the novel arm compared to the controls, indicating possible changes in the emotional and motivational states of the animals (novel latency: control, 7.22 ± 3.99 s, n = 16 vs. NIHL, 11.19 ± 6.02 s, n = 15, one-way ANOVA, $F(1,29) = 4.755$, $p = 0.037$; familiar latency: control, 20.53 ± 8.90 s, n = 15 vs. NIHL, 19.13 ± 6.98 s, n = 13, one-way ANOVA, $F(1,26) = 0.208$, $p = 0.652$). To investigate whether the increased latency to the first entry into the novel arm was because of a change in anxiety levels, we performed two well-validated

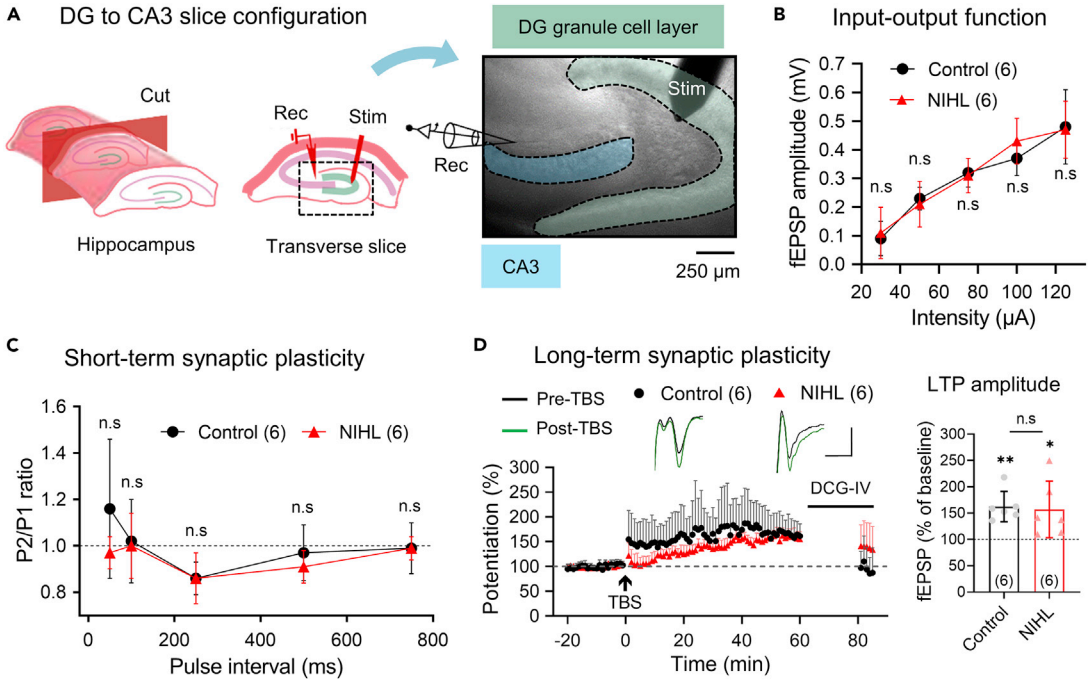


**Figure 2. NIHL minimally alters the DG-CA3 network**

(A) Hippocampal transverse slice preparation and configurations of the recording (Rec) and stimulating (Stim) electrodes in the slice used to examine the synaptic properties of the DG-CA3 network.

(B) The input-output function of CA3, represented as the fEPSP amplitude in response to increasing electrical stimulation of the DG granule cell layer, showed no significant differences between the control and NIHL groups.

(C) Short-term synaptic plasticity in response to a paired-pulse stimulation at various inter-pulse intervals. The P2/P1 (pulse2/pulse1) ratio is not significantly different between the control and NIHL groups.

(D) Long-term synaptic potentiation (LTP) at the DG-CA3 synapses, is induced by theta-burst stimulation (TBS). The insets display sample fEPSP traces of pre (black)- and post (green)-TBS induction (the scale bar denotes 5 ms × 0.2 mV). DCG-IV (mGluR2/3 agonist) is treated at the end of LTP experiment. The LTP amplitude is significantly increased compared to the normalized baseline (100%) in both groups and is not significantly different between the control and NIHL groups. The numbers in parentheses indicate the number of brain slices tested.

Data are presented as means ± SD. NIHL, noise-induced hearing loss; DG, dentate gyrus; fEPSP, field excitatory postsynaptic potential; *p < 0.05; **p < 0.01; n.s, not significant. Also, see Tables S2 and S3.

tests for anxiety: the open field test and the novelty-suppressed feeding test. In the NIHL group, the time (sec) ratio of the center zone to the outer zone in the open field test was reduced (control, 0.05 ± 0.03, n = 18 vs. NIHL, 0.04 ± 0.01, n = 13, one-way ANOVA, $F(1,29) = 4.364$, p = 0.046), whereas the total area traveled was unchanged (control, 30.44 ± 6.65 m, n = 18 vs. NIHL, 29.40 ± 6.14 m, n = 15, one-way ANOVA, $F(1,31) = 0.216$, p = 0.645) (Figure 1E). The latency to food biting in the novelty-suppressed feeding test was increased (control, 172.58 ± 89.78 s, n = 12 vs. NIHL, 267.45 ± 53.08 s, n = 11, one-way ANOVA, $F(1,21) = 9.284$, p = 0.006) (Figure 1F), These findings suggest that NIHL results in anxiety-like behaviors that have a negligible effect on short-term memory.

## NIHL minimally alters the DG-CA3 network

We next investigated the effects of NIHL on the DG-CA3 network, which is an important hippocampal circuit implicated in the modulation of anxiety levels (Ha et al., 2011; Seo et al., 2015). Transverse hippocampal slices were prepared, and recordings were acquired from the stratum lucidum (SL) within the CA3 region and with stimulation of the superior blade of the DGGC layer (Figure 2A). NIHL did not significantly change the synaptic input/output (I/O) function (repeated-measures two-way ANOVA, control vs. NIHL, $F(1,10) = 0.06$, p = 0.8104, see Table S2 for detail) (Figure 2B), and neither did short-term synaptic plasticity evoked by paired-pulse stimulation compared to the control (repeated-measures two-way ANOVA, control vs. NIHL, $F(1,10) = 1.187$, p = 0.301, see Table S3 for detail) (Figure 2C). Long-term potentiation (LTP) was reliably induced by theta burst stimulation (TBS) and did not significantly change the potentiation between the control and NIHL groups (control, 162.39 ± 28.82%, before vs. after TBS, paired $t$ test, $t = -5.303$, p = 0.003, n = 6; NIHL, 156.96 ± 53.82%,

before vs. after TBS, paired *t* test, $t = -2.592$, $p = 0.049$ n = 6; control vs. NIHL, both after TBS, one-way ANOVA, $F(1,10) = 0.048$, $p = 0.832$) (Figure 2D). Field excitatory postsynaptic potentials (fEPSPs) were suppressed by bath application of the group II-selective metabotropic glutamate receptor agonist, DCG-IV (20 μM) (control: 60 min, 161.19 ± 26.88%, n = 6 vs. 84 min, 83.46 ± 47.07%, n = 6, paired *t* test, $t(5) = 5.82$, $p = 0.002$, NIHL: 60 min, 156.53 ± 49.17%, n = 6 vs. 84 min, 134.46 ± 51.05, n = 6, paired *t* test, $t(5) = 3.10$, $p = 0.027$), indicating that the evoked potentials largely arise from DG-originated mossy fibers (Kamiya et al., 1996). These results show that the LTP magnitude in the transverse DG-CA3 is not significantly altered by NIHL.

## Longitudinal slicing angle preserves the intrinsic properties of DG granule neurons

The observation that NIHL did not alters long-term synaptic plasticity via transverse mossy fibers led us to consider another orientation of DG signal propagation, i.e., the longitudinal DG network along the dorsoventral axis perpendicular to the transverse projection. Based on the previous studies that suggested the existence of a longitudinal connection within the DG network (Lømo, 2009; Claiborne et al., 1986; Scharfman and Pierce, 2012; Jonas and Lisman, 2014; Choi et al., 2021), we examined the influence of NIHL on this network. We prepared longitudinal hippocampal slices by cutting the hippocampus along the dorsoventral axis to preserve longitudinal axons (Figure 3A) (Tetteh et al., 2019). Whole cell-patched DGGCs were identified based on the round shapes of their cell bodies, their relatively hyperpolarized RMPs, the dendritic spread toward the molecular layer, and their regular firing patterns in response to depolarizing current injection. To examine whether different slicing angles change the intrinsic properties of DGGCs, we measured their electrical properties in conventional transverse slices and longitudinal slices of the hippocampus. Whole-cell patch recordings of DGGCs showed that both the transverse and longitudinal slices had similarly linear relationships between the number of spikes and the depolarizing current injection (slope: transverse, 0.01314, n = 52 vs. longitudinal, 0.01623, n = 100, $F(1,214) = 0.2370$, $p = 0.6269$, ANCOVA) (Figure 3B) Notably, the longitudinal slices did not show any changes in RMP (longitudinal, −81.21 ± 8.71 mV, n = 24 vs. transverse, −77.29 ± 6.91 mV, n = 17, $F(1,39) = 2.266$, $p = 0.14$), input resistance (longitudinal, 344.13 ± 135.51 MΩ, n = 17 vs. transverse, 285.40 ± 206.19 MΩ, n = 16, $F(1,31) = 0.888$, $p = 0.353$), time constant (longitudinal, 0.02 ± 0.01 ms, n = 17 vs. transverse, 0.02 ± 0.01 ms, n = 15, $F(1,30) < 0.001$, $p = 0.993$), and threshold potential (longitudinal, −38.73 ± 5.96 mV, n = 10 vs. transverse, −43.36 ± 8.57 mV, n = 15, $F(1,23) = 2.031$, $p = 0.168$, one-way ANOVA, see Table S4 for detail) of DGGCs when compared with the transverse slices. Hence, any differences in the synaptic responses between the two orientations of hippocampal slices were not attributable to changes in the intrinsic membrane properties of presynaptic granule neurons caused by different slicing angles.

## Signals propagate longitudinally in the DG network

Given that longitudinal slices preserve the properties of DGGCs, we next tested whether electrical signals could be transferred along the longitudinal DG network. We recorded the sub-threshold responses and action potentials of whole-cell-patched DGGCs by stimulating the inner molecular layer (IML) of the superior blade of the DG (Figure 3C). 5 and 100 Hz stimulations successfully induced spikes, whereas a 100 Hz stimulation induced refractory periods in between the spike trains. By visualizing a single DGGC with two-photon imaging, we found that DGGCs not only have an axonal projection to CA3 but also have an axon pointing to the neighboring DG (306.80 ± 80.08 μm from the patched cell, n = 15) (Figure 3D). These results imply the existence of synaptic connections within the DG-DG network.

We further investigated whether the longitudinal axons of DG granule neurons have synaptic connections to neighboring DG granule neurons. Whole-cell patch-clamp recordings in longitudinal slices were acquired from the postsynaptic granule neurons, and caged glutamate was photolyzed in the presynaptic granule neurons to induce EPSPs in the postsynaptic neuron (176.80 ± 78.97 μm from the patched cell, n = 23) (Figure 3E). The EPSPs declined in the presence of 100 μM $Cd^{2+}$, which blocks synaptic transmission (before $Cd^{2+}$, 1.25 ± 0.6 mV vs. with $Cd^{2+}$, 0.21 ± 0.15 mV, paired *t* test, $t = 8.24$, $p < 0.0001$, n = 23 cells). These data demonstrate that the longitudinal projections of DG granule neurons retain functional synapses, supporting emerging evidence that DG networks, including granule and mossy cells, are synaptically wired to neighboring DG neurons in a longitudinal manner.

## Comparison of the synaptic properties of the DG-DG network in transverse and longitudinal slices of the hippocampus

Both longitudinal and transverse hippocampal slices were prepared with the stimulating and recording electrodes positioned near the borders of the molecular and granule cell layers (Figure 4A). The longitudinal

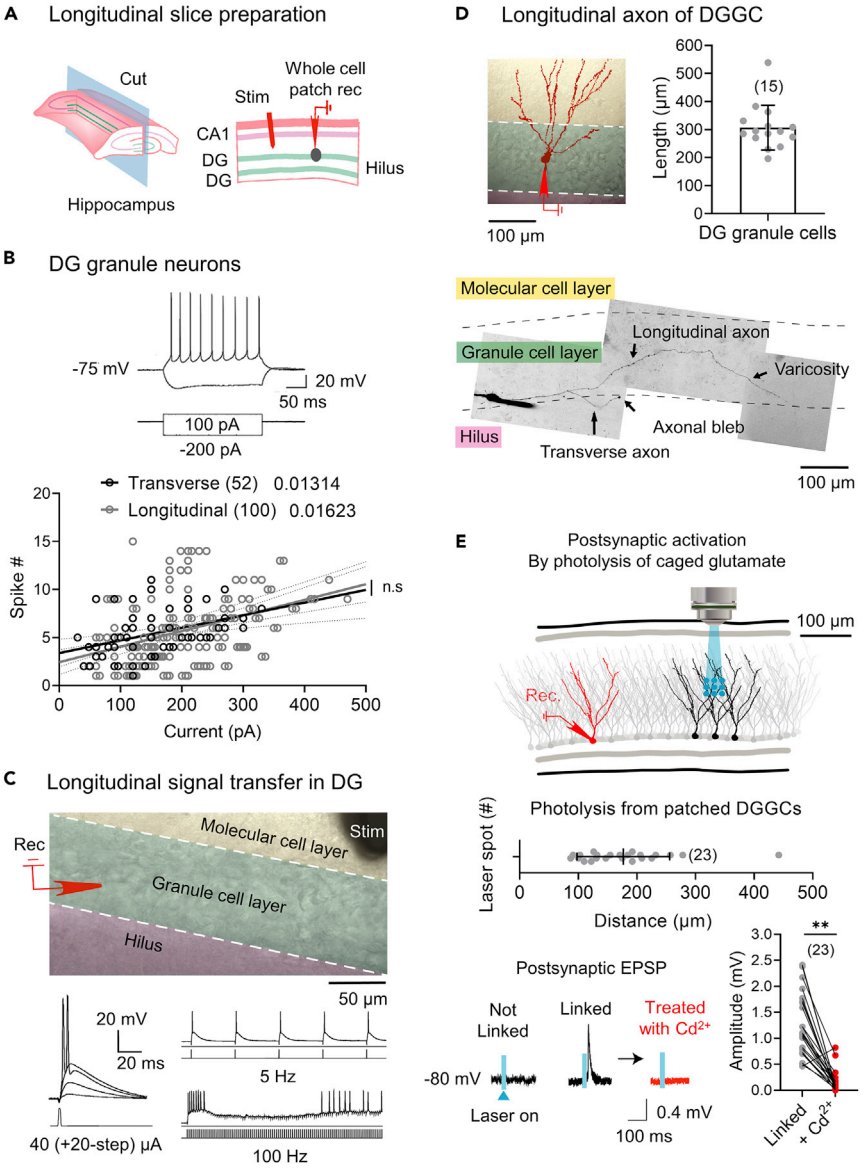


**Figure 3. Longitudinal slicing angle enables signals to propagate longitudinally in the DG network**

(A) Hippocampal longitudinal slice preparation and configuration of the stimulating (Stim) and recording (Rec) electrode and for whole-cell patch recording in the slice.

(B) DGGCs exhibit regular firing patterns in response to depolarizing current injection. The relationship between the number of spikes and the depolarizing current injection is similarly linear in both transverse and longitudinal slices. The floating numbers are positive progression slopes.

(C) The configurations of the recording and stimulating electrodes in hippocampal longitudinal slices when examining signal flow from the DG-DG network in the presence of picrotoxin (50 µM). The whole cell-patched DGGC generates sub-threshold responses and action potentials in response to increasing intensities of electrical stimulation in the molecular cell layer. The 5-Hz stimulation successfully induces spikes, and the 100-Hz stimulation induces refractory periods in the middle of the spike trains.

(D) The somatic and dendritic morphology of a DGGC, and a reconstructed image of a recorded DGGC filled with Alexa Fluor 594 showing axonal projections to the granule cell layer (a longitudinal axon) and to the hilus (a transverse axon).

(E) Glutamate uncaging is facilitated by local dot-photostimulation (cyan circle) of DGGCs that are hundreds of microns away from a patched cell (red) within the DG layer. Depolarization is induced in a postsynaptic patched neuron when it is linked to a presynaptic photo-activated neuron. Glutamate-induced EPSPs are far reduced in the presence of $Cd^{2+}$, which blocks synaptic transmission. The numbers in parentheses indicate the number of cells tested.

Data are presented as means ± SD. DG, dentate gyrus; DGGC, dentate gyrus granule cell; EPSP, excitatory postsynaptic potential; ** $p < 0.01$.

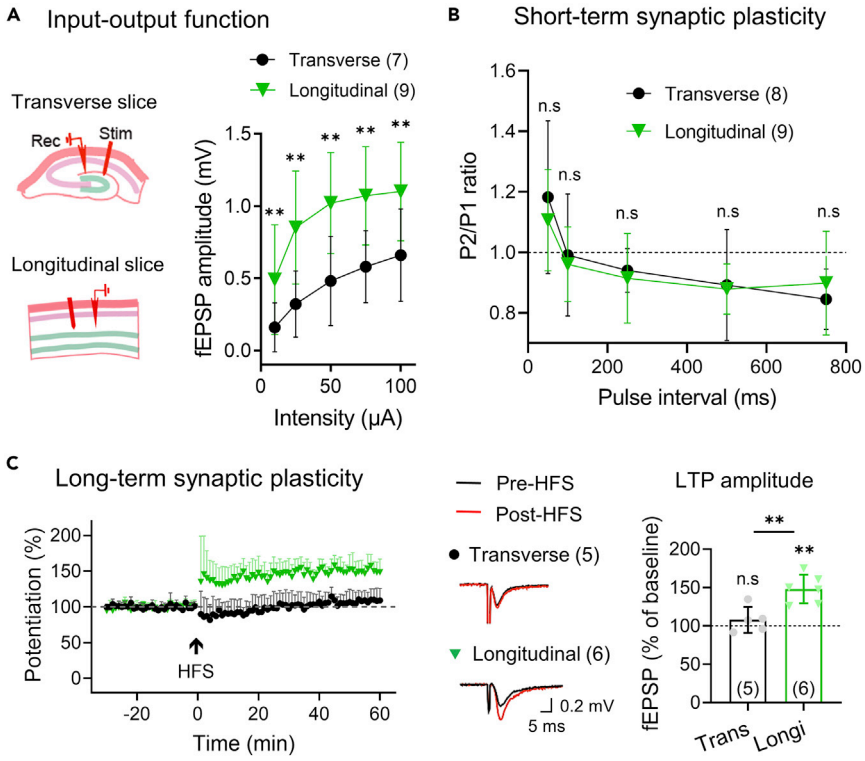


**Figure 4. Comparison of the synaptic properties of the DG-DG networks in transverse and longitudinal slices of the hippocampus**

(A) A schematic of the transverse and longitudinal slices of the hippocampus. Both longitudinal and transverse slices are prepared with stimulating (Stim) and recording (Rec) electrodes positioned near the borders of the molecular and granule cell layers. The input-output function of DG, represented as the fEPSP amplitude in response to increasing electrical stimulation of the DG granule cell layer, showed higher synaptic responsiveness in longitudinal slices than in transverse slices.

(B) Short-term synaptic plasticity in response to a paired-pulse stimulation at various inter-pulse intervals. The P2/P1 (pulse2/pulse1) ratio is not significantly different between the transverse and longitudinal slices.

(C) Long-term synaptic potentiation (LTP) in both preparations, is tested by high-frequency stimulation (HFS). The insets display sample fEPSP traces of pre (black)- and post (red)-HFS induction. The LTP amplitude in the longitudinal slices is significantly increased compared to the normalized baseline (100%) and is significantly different between the transverse and longitudinal slices. The numbers in parentheses indicate the number of brain slices tested.

Data are presented as means ± SD. DG, dentate gyrus; fEPSP, field excitatory postsynaptic potential; **p < 0.01. Also, see Tables S2 and S3.

slices showed higher synaptic responsiveness to a single stimulus that increased in intensity than the transverse slices (repeated-measures two-way ANOVA, longitudinal vs. transverse, $F(1,15) = 10.92$, $p = 0.0048$, see Table S2 for detail). Short-term synaptic plasticity, measured by the paired pulse response, showed no significant difference at various inter-pulse intervals (IPIs) between longitudinal and transverse slices, and paired-pulse depression was observed at the IPIs over 250 ms in both preparations (repeated-measures two-way ANOVA, longitudinal vs. transverse, $F(1,15) = 0.128$, $p = 0.725$, see Table S3 for detail) (Figure 4B)

We also found that high-frequency stimulation (HFS) of the IML induced LTP at the DG-DG synapses more reliably in the longitudinal slices than in the transverse slices (Figure 4C). Pronounced LTP was observed in the longitudinal slices (148.03 ± 18.66%, before vs. after HFS, paired *t* test, $t = -6.306$, $p = 0.001$, $n = 6$), and no LTP was observed in the transverse slices (107.89 ± 16.82%, before vs. after HFS, paired *t* test, $t = -1.049$, $p = 0.353$, $n = 8$; longitudinal vs. transverse, after HFS, one-way ANOVA, $F(1,9) = 13.771$, $p = 0.005$). These results suggest that the short- and long-term strengths of the longitudinal DG-DG connections are plastic.

## NIHL suppresses the synaptic plasticity of the DG-DG network

We next explored whether NIHL affects the synaptic properties of the DG-DG network. We used longitudinal hippocampal slices with the recording and stimulating electrodes placed in the molecular cell layer

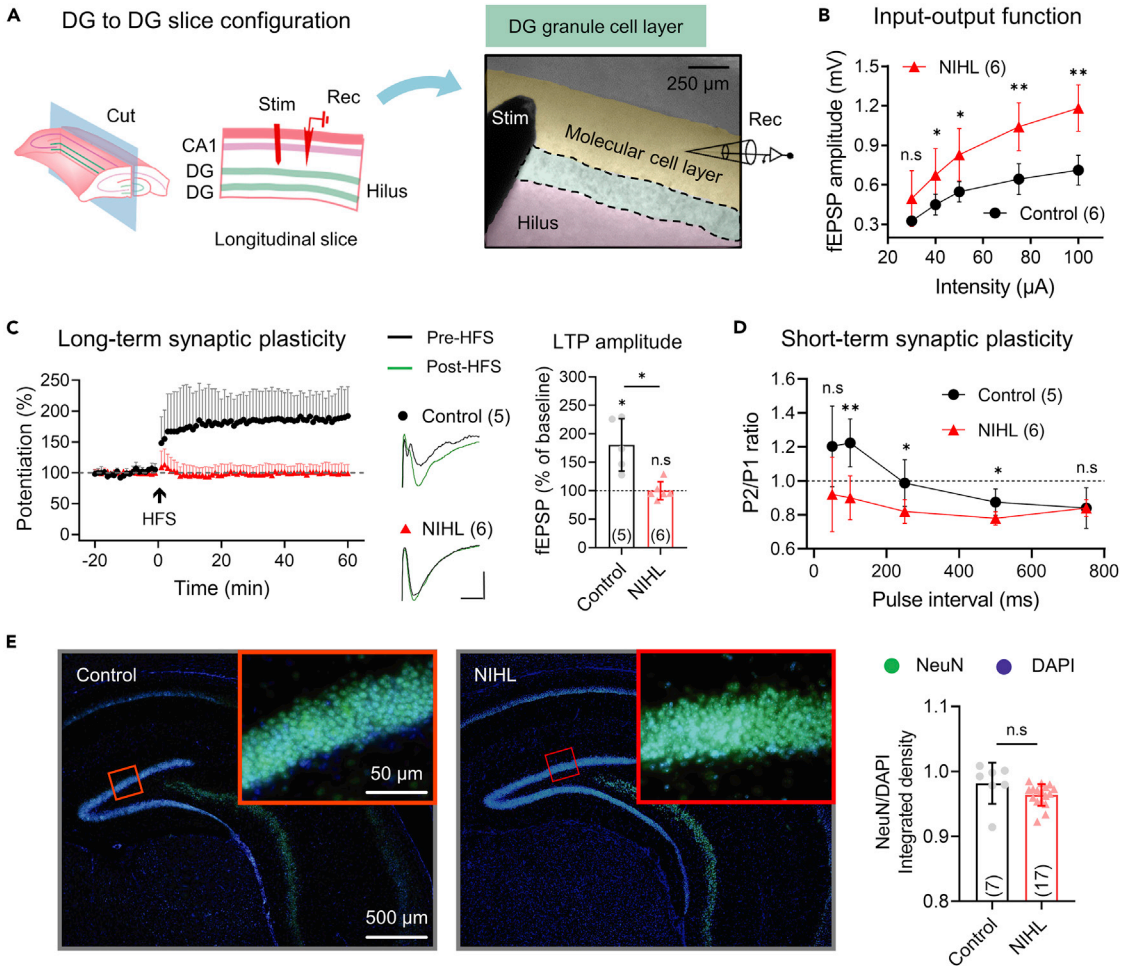


**Figure 5. NIHL suppresses synaptic plasticity in the longitudinal DG-DG network**

(A) Hippocampal longitudinal slice preparation and configurations of the stimulating (Stim) and recording (Rec) electrodes in the slice used to examine the synaptic properties of the DG-DG network.

(B) The input-output function of DG, represented as the fEPSP amplitude in response to increasing electrical stimulation of the inner molecular layer of the DG, shows hyperexcitable responses in the NIHL group.

(C) Long-term synaptic potentiation (LTP) at the DG-DG synapses, is induced by high-frequency stimulation (HFS). The insets display sample fEPSP traces of pre (black)- and post (green)-HFS induction (The scale bar denotes 5 ms × 0.2 mV). The LTP amplitude in the control group is significantly increased compared to the normalized baseline (100%) but not in the NIHL group and is significantly different between the control and NIHL groups. NIHL eliminates LTPs in the longitudinal DG network.

(D) Short-term synaptic plasticity in response to a paired-pulse stimulation at various inter-pulse intervals. The NIHL condition shows paired-pulse depression and is significantly more depressed than the control group in the P2/P1 (pulse2/pulse1) ratio.

(E) Immunohistochemistry to detect neuronal viability in the hippocampal DG, stained with an antibody against NeuN (green) and a stain of nuclear DNA (DAPI, blue). The relative NeuN integrated density (NeuN intensity normalized to the DAPI intensity) indicates no significant neuronal cell loss in the DG after NIHL. The numbers in parentheses indicate the number of brain slices tested.

Data are presented as means ± SD. NIHL: noise-induced hearing loss; DG, dentate gyrus; fEPSP, field excitatory postsynaptic potential; *p < 0.05; **p < 0.01; n.s, not significant. Also, see Tables S2 and S3.

(Figure 5A). Synaptic responsiveness to electrical stimuli was significantly higher in the NIHL slices than in the control slices, reflecting the NIHL-induced hyperexcitability of the DG-DG network (repeated-measures two-way ANOVA, control vs. NIHL, $F(1,10) = 11.36$, $p = 0.0071$, see Table S2 for detail) (Figure 5B). We then tested LTP in the longitudinal slices obtained from NIHL mice.

In NIHL mice, HFS failed to induce LTP in the longitudinal slices (control, 180.67 ± 45.96%, before vs. after HFS, paired *t* test, $t = -3.925$, $p = 0.017$, $n = 5$; NIHL, 100.04 ± 15.63%, before vs. after HFS, paired *t* test, $t = -0.007$, $p = 0.995$, $n = 6$; control vs. NIHL, after HFS, one-way ANOVA, $F(1,9) = 16.499$, $p = 0.033$)

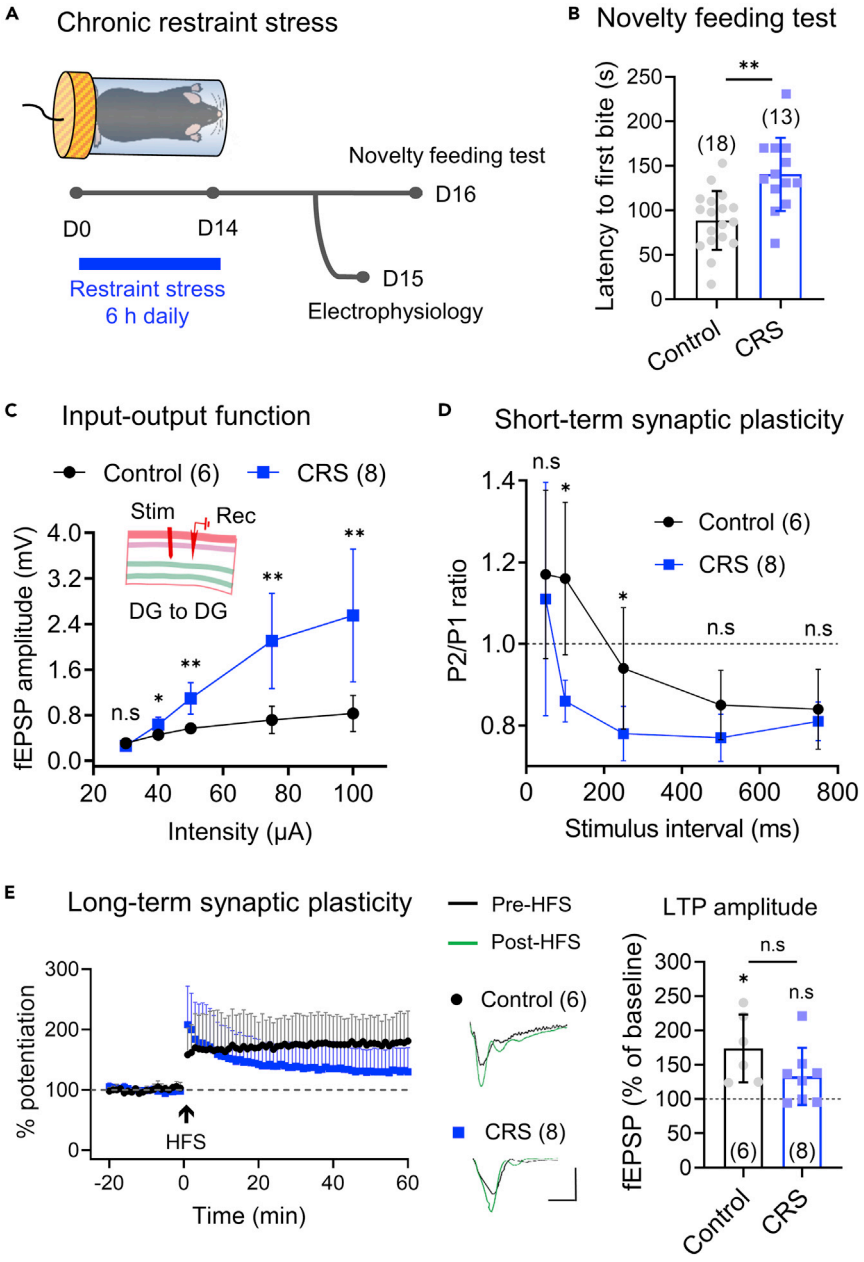


**Figure 6. Stress-induced anxiety alters synaptic plasticity in the longitudinal DG network**

(A) Schematic of a chronic stress-induced anxiety model and timeline of the experimental procedure.

(B) The latency to the first food bite in the novelty-suppressed feeding test. Chronic restraint stress (CRS) mice show increased latency to the first food bite and display anxiety-like behaviors. The numbers in parentheses indicate the number of animals tested.

(C) The input-output function of DG, represented as the fEPSP amplitude in response to increasing electrical stimulation of the inner molecular layer of the DG, shows hyperexcitable responses in the CRS group. The insert shows a hippocampal longitudinal slice and the configurations of the stimulating (Stim) and recording (Rec) electrodes when examining the synaptic properties of the DG-DG network.

(D) Short-term synaptic plasticity in response to a paired-pulse stimulation at various inter-pulse intervals. The CRS condition shows paired-pulse depression and is significantly more depressed than the control group in the P2/P1 (pulse2/pulse1) ratio.

(E) Long-term synaptic potentiation (LTP) at the DG-DG synapses, is induced by high-frequency stimulation (HFS). The insets display sample fEPSP traces of pre (black)- and post (green)-HFS induction (The scale bar denotes 5 ms × 0.2 mV). The LTP amplitude in the control group is significantly increased compared to the normalized baseline (100%) but not in

**Figure 6. *Continued***
the CRS group and is not significantly different between the control and CRS groups. CRS impairs LTPs in the longitudinal network. The numbers in parentheses indicate the number of brain slices tested.
Data are presented as means ± SD. DG, dentate gyrus; fEPSP, field excitatory postsynaptic potential; *p < 0.05; **p < 0.01; n.s: not significant. Also, see Tables S2 and S3.

(Figure 5C). Given that NIHL altered short-term synaptic plasticity by the paired-pulse ratios with varying intervals (repeated-measures two-way ANOVA, control vs. NIHL, $F(1,9) = 9.959$, $p = 0.012$, see Table S3 for detail) (Figure 5D), it is possible that the NIHL-induced disruption of LTPs involves presynaptic mechanisms. We also found no significant differences in the postsynaptic intrinsic membrane properties of DGGCs when compared with the controls (RMP: control, −81.57 ± 5.50 mV, n = 7 vs. NIHL, −84.17 ± 4.79 mV, n = 6, $F(1,11) = 0.807$, $p = 0.388$; time constant: control, 11.95 ± 3.86 ms, n = 7 vs. NIHL, 9.83 ± 2.67 ms, n = 6, $F(1,11) = 1.273$, $p = 0.283$; threshold current: control, 162.90 ± 31.47 pA, n = 7 vs. NIHL, 180 ± 21.91 pA, n = 6, $F(1,11) = 1.252$, $p = 0.287$; threshold potential: control, −37.43 ± 3.88 mV, n = 7 vs. NIHL, −37.27 ± 3.22 mV, n = 6, $F(1,11) = 0.006$, $p = 0.939$; input resistance: control, 175.3 ± 39.82 MΩ, n = 7 vs. NIHL, 156.7 ± 20.27 MΩ, n = 6, $F(1,11) = 1.06$, $p = 0.325$, one-way ANOVA, see Table S4 for detail).

Moreover, no neuronal cell loss was observed in the DGGC layers (control, 0.98 ± 0.03, n = 7 vs. NIHL, 0.96 ± 0.02, n = 17, one-way ANOVA, $F(1,22) = 3.397$, $p = 0.079$) (Figure 5E). These results demonstrate that NIHL suppresses synaptic plasticity in the DG-DG connection and that this suppression might strongly involve presynaptic alterations.

### Stress-induced anxiety alters the synaptic plasticity of the longitudinal DG-DG network

The chronic restraint stress (CRS) mouse model is widely used as a model of chronic psychoemotional stress for investigating anxiety-like behaviors (Huang et al., 2015). CRS does not change the short- and long-term plasticity of the CA3 in rodents upon mossy-fiber stimulation (Pavlides et al., 2002). Therefore, we examined whether CRS alters DG-DG synaptic plasticity in the context of anxiety. As previously described (Pavlides et al., 2002), CRS was induced by placing an animal in a 50-mL conical tube for 6 h per day for 14 consecutive days (Figure 6A). The latency to food biting significantly increased after CRS (control, 88.67 ± 33.06 s, n = 18 vs. CRS, 140.46 ± 41.15 s, n = 13, one-way ANOVA, $F(1,29) = 15.098$, $p = 0.001$), suggesting that CRS increases anxiety levels, as reported previously (Figure 6B) (Chiba et al., 2012). As seen in the NIHL model, the CRS mice showed hyperexcitable neuronal responses to electrical stimuli (repeated-measures two-way ANOVA, control vs. CRS, $F(1,13) = 16.43$, $p = 0.0014$, see Table S2 for detail) (Figure 6C). Paired-pulse depression was prominent at 100-ms and 250-ms stimulus intervals compared to the control (repeated-measures two-way ANOVA, control vs. CRS, $F(1,12) = 7.94$, $p = 0.016$, see Table S3 for detail) (Figure 6D). CRS also impaired the LTP induced by HFS (control, 173.23 ± 49.44%, before vs. after HFS, paired *t* test, $t = -3.857$, $p = 0.012$, n = 6; CRS, 132.92 ± 41.67%, before vs. after HFS, paired *t* test, $t = -2.277$, $p = 0.057$, n = 8; control vs. CRS, one-way ANOVA, $F(1,12) = 2.825$, $p = 0.119$) (Figure 6E). These results indicate that CRS increases anxiety levels in a manner similar to NIHL and alters the short- and long-term synaptic plasticity of the longitudinal DG-DG network.

## DISCUSSION

Anxiety disorders, such as post-traumatic stress disorder (PTSD) and specific phobia (SP), are typically characterized by an excessive fear response and/or worry (Edition, 2013). Functional neuroimaging studies report that activation of the hippocampus increases in response to threatening stimuli in PTSD and SP (Patel et al., 2012; Lueken et al., 2014; Garrett et al., 2012). In particular, manipulation of DGGC activity is associated with anxiety-like behaviors, suggesting that DGGCs contribute to regulating anxiety levels (Kheirbek et al., 2013). However, few studies have examined the role of the DG network in regulating anxiety at the synaptic and circuit levels.

Here, we demonstrate that an NIHL mouse model enhances anxious behavior and alters synaptic responsiveness in the longitudinal DG-DG network. To investigate a possible correlation between anxiety and the longitudinal DG-DG network, we compared a CRS-induced anxiety model with our NIHL-induced anxiety model. This was necessitated by our current inability to completely separate the longitudinal DG-DG network from the transverse DG-CA3 network. Both animal models with abnormal anxiety behaviors showed synaptic alterations in the DG-DG network, suggesting that these alterations are associated with behavioral

manifestations of anxiety but are not solely specific to NIHL. However, the dissimilarity in the trajectory of LTP progression might be resulted from the different pathophysiology of each animal model, presumably implicating that the synaptic alteration of the DG-DG network is more susceptible to NIHL than CRS.

Notably, NIHL-induced anxiety is not correlated with the transverse DG-CA3 network, which is known to underlie memory encoding. This may partially explain why our NIHL model does not show prominent memory impairment, as can be inferred from the results of the Y-maze and object-recognition tests. In addition, the CRS-induced anxiety model is not related to the mossy fibre-CA3 network, which is interchangeable with the transverse DG-CA3 network in rodents (Pavlides et al., 2002). Therefore, the DG-DG network could possibly predict anxiety-like behaviors.

The mechanisms by which such altered synaptic plasticity in the longitudinal network relates to anxiety at the circuit level need to be established. We speculate that, following hearing loss or chronic stress, the DG-DG network contributes to the rapid propagation of electrical signals, as evidenced by the hyperexcitable I/O function that is accompanied by paired-pulse depression. Subsequently, synaptic hyperexcitability of the DG-DG network could enhance the electrical spread to several cortices sequentially and/or simultaneously throughout the brain regions implicated in anxiety generation and/or development. Finally, this process could increase arousal and induce anxiety. However, it remains unclear whether anxiety renders the longitudinal DG network dysfunctional or whether a dysfunctional longitudinal DG network predisposes individuals to anxiety.

The hippocampus is susceptible to changes in response to noise exposure, irrespective of whether the noise is benign or traumatic. Long-term environmental noise exposure during the postnatal period (65 dB SPL) diminishes LTP in the perforant path (PP)-DG synapses and impairs hippocampus-dependent memory function (Zhang et al., 2021). Traumatic noise exposure (110–120 dB) also diminishes LTP in the CA3-CA1 and PP-DG networks, although the behavioral effects of such changes have not yet been studied (Cunha et al., 2015; De Deus et al., 2017). Our findings show that after traumatic noise, DG-CA3 synapses are not prominently altered in terms of short- and long-term plasticity. In contrast, the longitudinal DG-DG network is highly vulnerable to traumatic noise. This is closely associated with anxiety-like behavior but not with short-term memory impairment. Given that previous reports have shown memory impairment following either 3 months of post-acute noise exposure (Liu et al., 2018) or chronic repetitive noise exposure (Zhang et al., 2021), the 2-week observation period following acute noise exposure in our animal model may not be sufficient to reveal the development of a memory deficit. This difference between our study and previous studies presumably arises from disparities in the animal species (rats vs. mice), noise levels (circumstantial vs. traumatic), age (young vs. mature), and laterality (bilateral vs. unilateral).

Mossy cells are a prominent cell type in the hilus and actively interact with granule cells and interneurons in the DG. Some mossy cells have axonal projections that target the IML of the DG and run longitudinally along the dorsoventral hippocampus (Scharfman, 2016). Given the locations of the stimulating and recording electrodes, i.e., the middle molecular layer in the DG, their contributions to DG-DG activation appear to be minimal. Nonetheless, it is possible that the synaptic responses recorded in the middle molecular layer might reflect mossy axon-driven activities. There is also a possible synaptic effect of EC cells on the DG. Although the synaptic connection of the EC-DG circuitry is truncated during slice preparation, the severed axons must still possess the ability to be activated. Therefore, the synaptic responses we observed in the longitudinal DG-DG network may have been influenced by the axons of mossy and EC cells, albeit to a lesser degree. We can rule out the likelihood of inhibitory synaptic inputs to the DG-DG network, as all the experiments were performed in the presence of picrotoxin, a $GABA_A$ receptor antagonist. However, further investigations are required to separate the roles of the longitudinal axons of granule cells from those of the mossy cells in the DG. Despite these limitations, our study presents novel evidence of an association between a dysfunctional longitudinal DG network and enhanced anxiety behaviors. An abnormal longitudinal DG network is thus a potential hallmark of anxiety.

## Limitations of the study

As already noted in the discussion, the increased synaptic excitability may originate from presynaptic alteration of DG granule neurons as the membrane properties of postsynaptic neurons remained the same. However, it is still uncertain whether the synaptic response is solely from DG granule neurons and what types of presynaptic mechanisms are involved. It awaits future studies.

## STAR★METHODS

Detailed methods are provided in the online version of this paper and include the following:

- KEY RESOURCES TABLE
- RESOURCE AVAILABILITY
  - Lead contact
  - Materials availability
  - Data and code availability
- EXPERIMENTAL MODEL AND SUBJECT DETAILS
  - Animal models
- METHOD DETAILS
  - Auditory brainstem response (ABR) recording
  - Hippocampal brain slice preparation for electrophysiology
  - Whole-cell patch recording
  - Two-photon imaging and glutamate uncaging
  - Extracellular field recording
  - Immunohistochemistry
  - Behavioral tests
- QUANTIFICATION AND STATISTICAL ANALYSIS

## SUPPLEMENTAL INFORMATION

Supplemental information can be found online at https://doi.org/10.1016/j.isci.2022.104364.

## ACKNOWLEDGMENTS

This work was supported by the Incheon National University (International Cooperative) Research Grant for Sunggu Yang and the Research Grants Council of the Hong Kong Special Administrative Region (11102120) for Sungchil Yang.

## AUTHOR CONTRIBUTIONS

S.C.Y. and S.G.Y. conceptualized and designed the study. S.P., G.C., and J.L. performed the electrophysiology recordings. J.R., C.H.P., S.P., M.L., D.C., and L.W.L. performed the behavior test and analysis. G.C. performed the immunofluorescence. S.P. created the graphical abstract. S.G.Y, S.C.Y., and S.P. wrote the paper. S.G.Y, S.B, S.C.Y., L.W.L., and S.P. revised the paper. S.G.Y. and S.C.Y. acquired funding.

## DECLARATION OF INTERESTS

The authors declare no competing interests.

Received: October 6, 2021
Revised: January 31, 2022
Accepted: May 3, 2022
Published: June 17, 2022

## REFERENCES

Amaral, D.G., Scharfman, H.E., and Lavenex, P. (2007). The dentate gyrus: fundamental neuroanatomical organization (dentate gyrus for dummies). Prog. Brain Res. *163*, 3–790. https://doi.org/10.1016/s0079-6123(07)63001-5.

Anacker, C., Luna, V.M., Stevens, G.S., Millette, A., Shores, R., Jimenez, J.C., Chen, B., and Hen, R. (2018). Hippocampal neurogenesis confers stress resilience by inhibiting the ventral dentate gyrus. Nature *559*, 98–102. https://doi.org/10.1038/s41586-018-0262-4.

Bhatt, J.M., Bhattacharyya, N., and Lin, H.W. (2017). Relationships between tinnitus and the prevalence of anxiety and depression. Laryngoscope *127*, 466–469. https://doi.org/10.1002/lary.26107.

Blaabjerg, M., and Zimmer, J. (2007). The dentate mossy fibers: structural organization, development and plasticity. Prog. Brain Res. *163*, 85–803. https://doi.org/10.1016/s0079-6123(07)63005-2.

Chiba, S., Numakawa, T., Ninomiya, M., Richards, M.C., Wakabayashi, C., and Kunugi, H. (2012). Chronic restraint stress causes anxiety-and depression-like behaviors, downregulates glucocorticoid receptor expression, and attenuates glutamate release induced by brain-derived neurotrophic factor in the prefrontal cortex. Prog. Neuropsychopharmacol. Biol. Psychiatry *39*, 112–119. https://doi.org/10.1016/j.pnpbp.2012.05.018.

Choi, G., Kang, H., Chu, W., Yang, S., and Yang, S. (2021). Dynamics of longitudinal dentate gyrus axons associated with seizure. J. Physiol. *599*, 2273–2281. https://doi.org/10.1113/jp281056.

Claiborne, B.J., Amaral, D.G., and Cowan, W.M. (1986). A light and electron microscopic analysis of the mossy fibers of the rat dentate gyrus. J. Comp. Neurol. *246*, 435–458. https://doi.org/10.1002/cne.902460403.

Cunha, A., De Oliveira, J., Almeida, S., Garcia-Cairasco, N., and Leão, R. (2015). Inhibition of long-term potentiation in the schaffer-CA1 pathway by repetitive high-intensity sound stimulation. Neuroscience *310*, 114–127. https://doi.org/10.1016/j.neuroscience.2015.09.040.

de Deus, J.L., Cunha, A.O.S., Terzian, A.L., Resstel, L.B., Elias, L.L.K., Antunes-Rodrigues, J., Almeida, S.S., and Leão, R.M. (2017). A single episode of high intensity sound inhibits long-term potentiation in the hippocampus of rats. Sci. Rep. *7*, 14094–14113. https://doi.org/10.1038/s41598-017-14624-1.

Deal, J.A., Betz, J., Yaffe, K., Harris, T., Purchase-Helzner, E., Satterfield, S., Pratt, S., Govil, N., Simonsick, E.M., Lin, F.R., and Health, A.B.C.S.G. (2017). Hearing impairment and incident dementia and cognitive decline in older adults: the health ABC study. J. Gerontol. A. Biol. Sci. Med. Sci. *72*, 703–709. https://doi.org/10.1093/gerona/glw069.

Dinel, A.-L., Joffre, C., Trifilieff, P., Aubert, A., Foury, A., Le Ruyet, P., and Layé, S. (2014). Inflammation early in life is a vulnerability factor for emotional behavior at adolescence and for lipopolysaccharide-induced spatial memory and neurogenesis alteration at adulthood. J. Neuroinflammation *11*, 155. https://doi.org/10.1186/s12974-014-0155-x.

Blazer, D.G., and Tucci, D.L. (2019). Hearing loss and psychiatric disorders: a review. Psychol. Med. *49*, 891–897. https://doi.org/10.1017/S0033291718003409.

Edition, F. (2013). Diagnostic and Statistical Manual of Mental Disorders. Am Psychiatric Assoc. *21*, 591–643.

Garrett, A.S., Carrion, V., Kletter, H., Karchemskiy, A., Weems, C.F., and Reiss, A. (2012). Brain activation to facial expressions in youth with PTSD symptoms. Depress. Anxiety *29*, 449–459. https://doi.org/10.1002/da.21892.

Guitton, M.J. (2009). Tinnitus-provoking salicylate treatment triggers social impairments in mice. J. Psychosom. Res. *67*, 273–276. https://doi.org/10.1016/j.jpsychores.2008.10.017.

Snyder, J.S., Soumier, A., Brewer, M., Cameron, H.A., and Pickel, J. (2011). Adult hippocampal neurogenesis buffers stress responses and depressive behaviour. Nature *476*, 458–461. https://doi.org/10.1038/nature10287.

Hill, A.S., Sahay, A., and Hen, R. (2015). Increasing adult hippocampal neurogenesis is sufficient to reduce anxiety and depression-like behaviors. Neuropsychopharmacology *40*, 2368–2378. https://doi.org/10.1038/npp.2015.85.

Huang, P., Li, C., Fu, T., Zhao, D., Yi, Z., Lu, Q., Guo, L., and Xu, X. (2015). Flupirtine attenuates chronic restraint stress-induced cognitive deficits and hippocampal apoptosis in male mice. Behav. Brain Res. *288*, 1–10. https://doi.org/10.1016/j.bbr.2015.04.004.

Jonas, P., and Lisman, J. (2014). Structure, function, and plasticity of hippocampal dentate gyrus microcircuits. Front. Neural Circuits *8*, 107. https://doi.org/10.3389/fncir.2014.00107.

Kamiya, H., Shinozaki, H., and Yamamoto, C. (1996). Activation of metabotropic glutamate receptor type 2/3 suppresses transmission at rat hippocampal mossy fibre synapses. J. Physiol. *493*, 447–455. https://doi.org/10.1113/jphysiol.1996.sp021395.

Kheirbek, M.A., Drew, L.J., Burghardt, N.S., Costantini, D.O., Tannenholz, L., Ahmari, S.E., Zeng, H., Fenton, A.A., and Hen, R. (2013). Differential control of learning and anxiety along the dorsoventral axis of the dentate gyrus. Neuron *77*, 955–968. https://doi.org/10.1016/j.neuron.2012.12.038.

Koch, S.B.J., Morey, R.A., and Roelofs, K. (2020). The role of the dentate gyrus in stress-related disorders. Mol. Psychiatry *25*, 1361–1363. https://doi.org/10.1038/s41380-019-0572-4.

Kohara, K., Pignatelli, M., Rivest, A.J., Jung, H.Y., Kitamura, T., Suh, J., Frank, D., Kajikawa, K., Mise, N., Obata, Y., et al. (2014). Cell type-specific genetic and optogenetic tools reveal hippocampal CA2 circuits. Nat. Neurosci. *17*, 269–279. https://doi.org/10.1038/nn.3614.

Lauer, A.M., Larkin, G., Jones, A., and May, B.J. (2018). Behavioral animal model of the emotional response to tinnitus and hearing loss. J. Assoc. Res. Otolaryngol. *19*, 67–81. https://doi.org/10.1007/s10162-017-0642-8.

Leung, C., Cao, F., Nguyen, R., Joshi, K., Aqrabawi, A.J., Xia, S., Cortez, M.A., Snead, O.C., Iii, Kim, J.C., and Jia, Z. (2018). Activation of entorhinal cortical projections to the dentate gyrus underlies social memory retrieval. Cell Rep. *23*, 2379–2391. https://doi.org/10.1016/j.celrep.2018.04.073.

Lim, L.W., Shrestha, S., Or, Y.Z., Tan, S.Z.K., Chung, H.H., Sun, Y., Lim, C.L., Khairuddin, S., Lufkin, T., and Lin, V.C.L. (2016). Tetratricopeptide repeat domain 9A modulates anxiety-like behavior in female mice. Sci. Rep. *6*, 37568. https://doi.org/10.1038/srep37568.

Liu, L., Xuan, C., Shen, P., He, T., Chang, Y., Shi, L., Tao, S., Yu, Z., Brown, R.E., and Wang, J. (2018). Hippocampal mechanisms underlying impairment in spatial learning long after establishment of noise-induced hearing loss in CBA mice. Front. Syst. Neurosci. *12*, 35. https://doi.org/10.3389/fnsys.2018.00035.

Lømo, T. (2009). Excitability changes within transverse lamellae of dentate granule cells and their longitudinal spread following orthodromic or antidromic activation. Hippocampus *19*, 633–648. https://doi.org/10.1002/hipo.20538.

Lueken, U., Hilbert, K., Stolyar, V., Maslowski, N.I., Beesdo-Baum, K., and Wittchen, H.-U. (2014). Neural substrates of defensive reactivity in two subtypes of specific phobia. Soc. Cogn. Affect. Neurosci. *9*, 1668–1675. https://doi.org/10.1093/scan/nst159.

Manohar, S., Adler, H.J., Chen, G.-D., and Salvi, R. (2020). Blast-induced hearing loss suppresses hippocampal neurogenesis and disrupts long term spatial memory. Hear. Res. *395*, 108022. https://doi.org/10.1016/j.heares.2020.108022.

Nadhimi, Y., and Llano, D.A. (2021). Does hearing loss lead to dementia? A review of the literature. Hear. Res. *402*, 108038. https://doi.org/10.1016/j.heares.2020.108038.

Nelson, D.I., Nelson, R.Y., Concha-Barrientos, M., and Fingerhut, M. (2005). The global burden of occupational noise-induced hearing loss. Am. J. Ind. Med. *48*, 446–458. https://doi.org/10.1002/ajim.20223.

Pare, D., and Llinas, R. (1994). Non-lamellar propagation of entorhinal influences in the hippocampal formation: multiple electrode recordings in the isolated Guinea pig brain in vitro. Hippocampus *4*, 403–409. https://doi.org/10.1002/hipo.450040403.

Patel, R., Spreng, R.N., Shin, L.M., and Girard, T.A. (2012). Neurocircuitry models of posttraumatic stress disorder and beyond: a meta-analysis of functional neuroimaging studies. Neurosci. Biobehav. Rev. *36*, 2130–2142. https://doi.org/10.1016/j.neubiorev.2012.06.003.

Pavlides, C., Nivón, L.G., and Mcewen, B.S. (2002). Effects of chronic stress on hippocampal long-term potentiation. Hippocampus *12*, 245–257. https://doi.org/10.1002/hipo.1116.

Scharfman, H.E., and Pierce, J.P. (2012). New insights into the role of hilar ectopic granule cells in the dentate gyrus based on quantitative anatomic analysis and three-dimensional reconstruction. Epilepsia *53*, 109–115. https://doi.org/10.1111/j.1528-1167.2012.03480.x.

Scharfman, H.E. (2016). The enigmatic mossy cell of the dentate gyrus. Nat. Rev. Neurosci. *17*, 562–575. https://doi.org/10.1038/nrn.2016.87.

Schneider, C.A., Rasband, W.S., and Eliceiri, K.W. (2012). NIH Image to ImageJ: 25 years of image analysis. Nat. Methods *9*, 671–675. https://doi.org/10.1038/nmeth.2089.

Seo, D.-O., Carillo, M.A., Chih-Hsiung Lim, S., Tanaka, K.F., and Drew, M.R. (2015). Adult hippocampal neurogenesis modulates fear learning through associative and nonassociative mechanisms. J. Neurosci. *35*, 11330–11345. https://doi.org/10.1523/jneurosci.0483-15.2015.

Sun, D.G., Kang, H., Tetteh, H., Su, J., Lee, J., Park, S.W., He, J., Jo, J., Yang, S., and Yang, S. (2018). Long term potentiation, but not depression, in interlamellar hippocampus CA1. Sci. Rep. *8*, 5187. https://doi.org/10.1038/s41598-018-23369-4.

Swanson, L.W., Wyss, J.M., and Cowan, W.M. (1978). An autoradiographic study of the organization of intrahippocampal association pathways in the rat. J. Comp. Neurol. *181*, 681–715. https://doi.org/10.1002/cne.901810402.

Tetteh, H., Lee, J., Lee, J., Kim, J.G., and Yang, S. (2019). Investigating long-term synaptic plasticity in interlamellar hippocampus CA1 by electrophysiological field recording. JoVE *11*, e59879. https://doi.org/10.3791/59879.

Weeden, C.S., Roberts, J.M., Kamm, A.M., and Kesner, R.P. (2015). The role of the ventral dentate gyrus in anxiety-based behaviors. Neurobiol. Learn. Mem. *118*, 143–149. https://doi.org/10.1016/j.nlm.2014.12.002.

Yalcin, I., Bohren, Y., Waltisperger, E., Sage-Ciocca, D., Yin, J.C., Freund-Mercier, M.-J., and Barrot, M. (2011). A time-dependent history of mood disorders in a murine model of neuropathic pain. Biol. Psychiatry *70*, 946–953. https://doi.org/10.1016/j.biopsych.2011.07.017.

Yang, S., and Bao, S. (2013). Homeostatic mechanisms and treatment of tinnitus. Restor. Neurol. Neurosci. *31*, 99–108. https://doi.org/10.3233/rnn-120248.

Yang, S., Moreira, T., Hoffman, G., Carlson, G.C., Bender, K.J., Alger, B.E., and Tang, C.M. (2014a). Interlamellar CA1 network in the hippocampus. Proc. Natl. Acad. Sci. U S A *111*, 12919–12924. https://doi.org/10.1073/pnas.1405468111.

Yang, S., Santos, M.D., Tang, C.-M., Kim, J.G., and Yang, S. (2016). A postsynaptic role for short-term neuronal facilitation in dendritic spines. Front. Cell. Neurosci. *10*, 224. https://doi.org/10.3389/fncel.2016.00224.

Yang, S., Yang, S., Moreira, T., Hoffman, G., Carlson, G.C., Bender, K.J., Alger, B.E., and Tang, C.-M. (2014b). Interlamellar CA1 network in the hippocampus. Proc. Natl. Acad. Sci. U S A *111*, 12919–12924. https://doi.org/10.1073/pnas.1405468111.

Zhang, Y., Zhu, M., Sun, Y., Tang, B., Zhang, G., An, P., Cheng, Y., Shan, Y., Merzenich, M.M., and Zhou, X. (2021). Environmental noise degrades hippocampus-related learning and memory. Proc. Natl. Acad. Sci. U S A *118*. e2017841117. https://doi.org/10.1073/pnas.2017841117.

Zheng, Y., Hamilton, E., Mcnamara, E., Smith, P., and Darlington, C. (2011). The effects of chronic tinnitus caused by acoustic trauma on social behaviour and anxiety in rats. Neuroscience *193*, 143–153. https://doi.org/10.1016/j.neuroscience.2011.07.026.

Zou, D., Chen, L., Deng, D., Jiang, D., Dong, F., Mcsweeney, C., Zhou, Y., Liu, L., Chen, G., Wu, Y., and Mao, Y. (2016). DREADD in parvalbumin interneurons of the dentate gyrus modulates anxiety, social interaction and memory extinction. Curr. Mol. Med. *16*, 91–102. https://doi.org/10.2174/1566524016666151222150024.

## STAR★METHODS

### KEY RESOURCES TABLE

| REAGENT or RESOURCE | SOURCE | IDENTIFIER |
|---|---|---|
| **Antibodies** | | |
| Mouse monoclonal anti-NeuN | Abcam | Cat# ab104224; RRID: AB_10711040 |
| Secondary antibodies conjugated with Alexa Fluor 488 | Jackson Immunoresearch | Cat#: 115-545-205; RRID: AB_2338854 |
| **Chemicals, peptides, and recombinant proteins** | | |
| Ketamine 10% | Alfasan International B.V | https://www.alfasan.com/en/ |
| Xylazine 2% | Alfasan International B.V | https://www.alfasan.com/en/ |
| Isoflurane | RWD Life Science | R510-22 |
| Sucrose | Sigma-Aldrich | S0389 |
| NaCl | Sigma-Aldrich | S7653 |
| KCl | Sigma-Aldrich | P9333 |
| $NaH_2PO_4$ | Sigma-Aldrich | S5011 |
| $NaHCO_3$ | Sigma-Aldrich | S6297 |
| Glucose | Sigma-Aldrich | G8270 |
| $MgCl_2$ | Sigma-Aldrich | M2670 |
| $CaCl_2$ | Sigma-Aldrich | C8106 |
| K-gluconate | Sigma-Aldrich | P1847 |
| EGTA | Sigma-Aldrich | E0396 |
| HEPES | Sigma-Aldrich | H7523 |
| $Na_2$-ATP | Sigma-Aldrich | A9187 |
| Na-GTP | Sigma-Aldrich | G8877 |
| Alexa Fluor 594 | Tocris | A10438 |
| MNI-caged-L-glutamate | Tocris | 1490 |
| $CdCl_2$ | Sigma-Aldrich | 655,198 |
| Picrotoxin | Sigma-Aldrich | P1675 |
| DCG-IV | Tocris | 0975 |
| DAPI | Santa Cruz | sc-3598 |
| Vectashield | Vector Labs | H-1000-10 |
| **Experimental models: Organisms/strains** | | |
| Mouse: C57BL/6J | The Jackson Laboratory | 000664 |
| **Software and algorithms** | | |
| MATLAB | The MathWorks, Inc. | https://www.mathworks.com/ |
| BioSigRZ | Tucker-Davis Technologies | https://www.tdt.com/ |
| pCLAMP software | Molecular Devices | v10.2 |
| Image J | (Schneider et al., 2012) | https://imagej.nih.gov/ij/ |
| ANY-maze software | ANY-maze | https://www.any-maze.com/ |
| GraphPad Prism 8.02 | GraphPad Software | https://www.graphpad.com/ |
| **Other** | | |
| MF1 multi-field magnetic speaker | Tucker-Davis Technologies | https://www.tdt.com/ |
| Power amplifier | Samson Technologies | 120a |
| ICP microphone system | PCB Piezotronics | 378B02 |

(*Continued on next page*)

*Continued*

| REAGENT or RESOURCE | SOURCE | IDENTIFIER |
|---|---|---|
| Tucker-Davis Technologies System 3 hardware (Medusa PreAmps, RZ6 Multi I/O Processor, MF1 multi-field magnetic speaker) | Tucker-Davis Technologies | https://www.tdt.com/ |
| Three-needle electrodes | Rochester | S83018-R9 |
| Temperature controller | RWD Life Science | https://www.rwdstco.com/ |
| Vibratome | Leica Biosystems | VT1200S |
| Recording chamber | Warner Instruments | RC-26GLP |
| Axon Instruments MultiClamp 700B Amplifier | Molecular Devices | https://www.moleculardevices.com/ |
| Ti-sapphire laser | Coherent Chameleon | https://www.coherent.com/ |
| Concentric bipolar microelectrode | FHC Inc | CBAPC75 |

## RESOURCE AVAILABILITY

### Lead contact

Further information and requests for resources and reagents should be directed to and will be fulfilled by the lead contact, Sungchil yang (sungchil.yang@cityu.edu.hk).

### Materials availability

This study did not generate new unique reagents.

### Data and code availability

All data produced in this study are included in the published article and its supplementary information, or are available from the lead contact upon request. This paper does not report original code. Any additional information required to reanalyze the data reported in this paper is available from the lead contact upon request.

## EXPERIMENTAL MODEL AND SUBJECT DETAILS

### Animal models

Male C57BL/6J mice aged 8–14 weeks were housed under a 12-h light/12-h dark cycle in a temperature-controlled environment (23 °C) and allowed access to food and water *ad libitum*. For the noise-induced hearing loss (NIHL) model, all experiments were performed on mice anesthetized by an intraperitoneal (IP) injection of 100 mg ketamine/kg and 10 mg xylazine/kg based on their body weights. One-third of the initial dose was additionally delivered by IP injection as necessary. A unilateral hearing lesion was induced by traumatic noise exposure for 2 h on day 0 (Pre) in the left ears of the animals. The noise (continuous pure tone of 8 kHz at 115 dB sound pressure level [SPL]) was played via a customized MATLAB program through a closed-field magnetic speaker (MF1 multi-field magnetic speaker, Tucker-Davis Technologies) amplified by a Samson Servo 120a amplifier (Samson Technologies, Hicksville, NY). The level of traumatizing tone was measured with an ICP microphone system (378B02, PCB Piezotronics, NY, USA) and calibrated with a customized LabVIEW 2019 software. The opposing (right) ears were plugged with cotton swabs to preserve function during hearing lesioning. Sham control mice underwent anesthesia for 2 h without sound exposure. Because noise stimuli were delivered to the left ears, the hippocampus contralateral to the noise-exposed ears was chosen for electrophysiological recordings. The noise-exposed and sham control mice were housed after anesthesia in individual cages for approximately 10 days before conducting the behavioral and electrophysiological measurements. Chronic restraint stress (CRS) was induced by placing the animals in 50-mL conical tubes with multiple ventilation holes at their home cages for 6 h a day for 14 consecutive days. Mice in the non-CRS group were simultaneously deprived of food and water but not subjected to restraint. Following hearing lesions or restraint stress, the animals were continuously monitored for pain/stress. If any signs of pain/stress were observed, analgesics (buprenorphine 0.05 mg/kg) were administered as necessary. All animal handling procedures were approved by the Institutional Animal Care and Use Committee of City University of Hong Kong (A-0117) and Incheon National University (INU-ANIM-2017-08). This research complies with all the guidelines of our institution's animal welfare committee and this journal's ethics policies.

## METHOD DETAILS

### Auditory brainstem response (ABR) recording

ABR recordings were used to assess hearing sensitivity before and 7 days after the noise exposure (pre and day 7, respectively). Sound generation and ABR recordings were performed using Tucker-Davis Technologies System 3 hardware (Medusa Pre-Amps, RZ6 Multi I/O Processor, MF1 multi-field magnetic speaker, FL, USA) and software (BioSigRZ, FL, USA). Acoustic stimuli were delivered through a closed-field magnetic speaker (MF1 multi-field magnetic speaker, Tucker-Davis Technologies) and were constituted of tone-pips (5-ms full-cycle sine waves) of various frequencies (4 kHz, 8 kHz, 16 kHz, and 32 kHz), each of which was played at intensities of 80–10 dB in decrements of 10 dB. Sound-evoked bioelectrical potentials were recorded using three-needle electrodes (S83018-R9, Rochester) placed subcutaneously in the test ear (active), the vertex of the head (ground), and the contralateral ear (reference). Hearing thresholds were evaluated by visually inspecting the ABR waveforms and defined as the lowest sound intensity at which a distinct first wave was observed. For convenience of calculation, the threshold was set up at 90 dB when no sound-evoked waveform was observed at 80 dB. The animals' body temperature was maintained at 37 °C during the entire procedure using a temperature controller (RWD Life Science), and dryness of the animals' eyes was prevented using tear ointment.

### Hippocampal brain slice preparation for electrophysiology

The brain preparation and electrophysiology procedures have been described in detail in the previous publication (Sun et al., 2018). Briefly, male C57BL/6J mice aged 8–14 weeks (~4 weeks for comparing transverse and longitudinal slices) were deeply anesthetized with isoflurane. The brains were quickly removed and placed into chilled (4 °C) and oxygenated (5% $CO_2$ and 95% $O_2$) slicing medium containing 75 mM sucrose, 87 mM NaCl, 2.5 mM KCl, 1.3 mM $NaH_2PO_4$, 25 mM $NaHCO_3$, 25 mM glucose, 7 mM $MgCl_2$ and 0.5 mM $CaCl_2$. Transverse slices were cut perpendicular to the dorsoventral axis of the hippocampus, and longitudinal slices were cut parallel to the dorsoventral plane. 300-μm-thick slices were for whole-cell patch recording and 400-μm-thick slices were for extracellular field recording. The brain slices were then transferred to a holding chamber containing oxygenated artificial cerebrospinal fluid (ACSF; 125 mM NaCl, 2.5 mM KCl, 1.3 mM $NaH_2PO_4$, 25 mM $NaHCO_3$, 25 mM glucose, 1 mM $MgCl_2$, and 2 mM $CaCl_2$). After ~30 min of recovery at 32 °C, followed by at least 0.5 h at room temperature (whole-cell patch recording) or at least 1 h at room temperature (extracellular field recording), the slices in the recording chambers (Warner, MA) were submerged in ACSF (32 °C) delivered at a flow rate of 1.5 mL/min and bubbled with a mixture of 95% $O_2$ and 5% $CO_2$.

### Whole-cell patch recording

The whole-cell patch recording procedures have been described in detail in our previous publications (Yang et al., 2016). Briefly, the transverse or longitudinal hippocampal slices were transferred from the holding beakers to the recording chambers and were submerged in ACSF (32 °C) with a mixture of 95% O2 and 5% CO2. Whole-cell patch recordings were obtained using an Axon Instruments Multi-Clamp 700B Amplifier (Molecular Devices); the recording pipettes had tip resistances of 5–7 MΩ and were filled with a solution containing (in mM) 135 K-gluconate, 5 KCl, 1 $MgCl_2$, 0.02 $CaCl_2$, 0.2 EGTA, 10 HEPES, 4 $Na_2$-ATP and 0.3 Na-GTP. Alexa Fluor 594 (20–50 μM, Tocris) was included in the internal solution for morphological visualization as required. The pH and osmolarity of the intracellular solution were adjusted to 7.3 and 290 mOsm, respectively. The initial serial resistance typically ranged from 9 MΩ to 17 MΩ and was maintained at a stable value during the recording sessions. Serial resistances were also continuously monitored with a brief voltage pulse and were not compensated. Recordings were acquired when the cells showed serial resistance with <25% fluctuation during the recording sessions. pCLAMP v10.2 software (Molecular Devices) was used for data acquisition and analysis. To measure the neurons' intrinsic properties, the resting membrane potential (RMP) was measured using the cells' resting state membrane potential 1 min after whole-cell configuration was achieved. The cells' input resistances were calculated from their steady-state membrane potentials, i.e., from the voltage changes induced by small hyperpolarizing current pulses (−20 pA). The membrane time constant represents the time required for the voltage to reach 63% of the peak value and was determined by fitting exponential curves to the hyperpolarized voltage responses. The threshold potential (mV) was visually determined at the voltage level, which showed a sudden increase in the slope of the action potential. The threshold current (pA) was determined at the lowest current level injected to induce a single action potential. To evoke synaptic potentials of a patched DGGC on the longitudinal slice, a stimulating electrode of the concentric bipolar microelectrode (CBAPC75, 25 mm inner

pole diameter, FHC, USA) was placed in the inner molecular layer (IML) hundreds of microns away from a patched cell. 5 and 100 Hz stimulations were delivered to ensure synaptic connections between DGGCs.

### Two-photon imaging and glutamate uncaging

The procedure for two-photon imaging has been described in detail in our previous publications (Yang et al., 2014b). Briefly, a Ti-sapphire laser was tuned to 810 nm (Coherent Chameleon) for morphological visualization with Alexa 594. Epi-fluorescent and trans-fluorescent signals were captured through a 60×, 1.0 N.A. objective and a 1.4 N.A. oil-immersion condenser (Olympus). The fluorescence was split into red and green channels using dichroic mirrors and band-pass filters. Red fluorescence (Alexa 594) signals were captured using R9110 photomultiplier tubes. For glutamate uncaging, another Ti-sapphire laser was tuned to 720 nm (Coherent Chameleon) to release the 4-methoxy-7-nitroindolinyl (MNI) compound from glutamate. MNI-caged-L-glutamate (Tocris) was prepared each day freshly at the final concentration (500 μM) in the physiological solution. The 3 × 3 grid of point stimulation (5 ms laser duration, 10 μm spot spacing, and various interpoint delay, > 0.12 ms) at an average power of 42 mW (ranged from 7.5 to 78.08 mW) was performed using Prairie View 5.4 software (Bruker Corporation); each spot size ranged from a diffraction-limited spot 0.2 to 1 μm (with laser intensity and objective dependency). Cadmium chloride ($CdCl_2$; 0.1 mM) was externally applied to the brain slices to block chemical synaptic transmission at the presynaptic terminals.

### Extracellular field recording

The transverse or longitudinal hippocampal slices were transferred from the holding beakers to the recording chambers and were submerged in ACSF (32 °C) bubbled with a mixture of 95% O2 and 5% CO2. In all extracellular field recordings, picrotoxin (50 μM; Sigma) was applied to the perfusate 15–20 min before the recordings were acquired. Local field potentials (LFPs) were evoked (constant current, 100 μs duration, repeated at 30-s intervals) in the transverse slices by placing a stimulating electrode (concentric bipolar microelectrode, CBAPC75, 25 mm inner pole diameter, FHC, USA) in the superior blade of the DGGC layer. LFPs were then recorded from the stratum lucidum (SL) within the CA3 region using glass electrodes containing ACSF. Long-term potentiation (LTP) was induced by theta-burst stimulation (TBS; 10 trains of 4-pulse bursts at 100 Hz, 200-ms inter-burst interval, delivered at 0.1 Hz). At the end of the experiment, the group II-selective metabotropic glutamate receptor (mGluR2/3) agonist DCG-IV (20 μM, Sigma-Aldrich, St Louis, MO) was bath-applied to examine the involvement of mossy fibers in the synaptic responses.

For the longitudinal slices, the recording and stimulating electrodes were placed in the middle molecular layer along the longitudinal axis to record and evoke LFPs (constant current, 100 μs duration, repeated at 30-s intervals). Long-term synaptic plasticity (i.e., LTP) was induced by 4 trains of tetanus stimuli (high-frequency stimulation [HFS]; 100 Hz, 1 s, 4 times at 1-s intervals) after acquiring >20 min of stable baseline recordings.

The peak amplitudes of all LFPs were analyzed offline using Clampfit software (Axon Instruments). Before LTP was induced, the input/output (I/O) curves and paired-pulse responses were identified. The short (paired-pulse response)- and long (LTP)-term synaptic plasticity were recorded using stimulation intensities producing half-maximal response amplitudes. The Pulse 2 (P2)/Pulse 1 (P1) ratio of paired-pulse responses was calculated by the peak amplitude of the second LFP divided by that of the first LFP measured at inter-pulse intervals of 50 ms, 100 ms, 250 ms, 500 m, and 750 ms. Any changes in synaptic strength (i.e., LTP) were expressed relative to the pre-conditioning baseline normalized to 100%. Averaged LFP amplitude during the last 10 min of baseline recording was compared to that during the last 10 min of post-conditioning recording.

### Immunohistochemistry

After the animals were transcardially perfused with phosphate-buffered saline (PBS) and 4% paraformaldehyde (PFA), the isolated brains were immersed overnight at 4 °C in a centrifuge tube containing 4% PFA in 120 mM phosphate buffer, maintained at pH 7.4. A Leica VT1000 S vibrating blade microtome (Leica Biosystems) was used to cut 100-μm thick coronal sections, which were treated with blocking solution for 30 min at room temperature (125 mL PBS, 2.5 mL 10% Triton X-100, 1.25 mL 20% $NaN_3$ [w/v], 100% serum [normal goat serum; NGS or normal donkey serum; NDS], and PBS to a total volume of 250 mL) to block and permeabilize the sections. The mouse monoclonal anti-NeuN antibody was used as a neuronal marker

(1:250; Abcam, ab104224). The sections were incubated for 24 h at 4 °C with the primary antibodies and then incubated with the corresponding secondary antibodies conjugated with Alexa Fluor 488 (1:500; Jackson Immunoresearch, 115-545-205) and 4′,6-diamidino-2-phenylindole (DAPI, Santa Cruz, sc-3598) for 1 h at room temperature. After rinsing with PBS, the sections were mounted with Vectashield (Vector Labs) and viewed under a fluorescence microscope (Nikon Eclipse Ni-E). The right hemisphere of the hippocampus, contralateral to the noise-exposed ear, was chosen for analysis. The integrated densities (i.e., the sum of all pixels in the ROI) of the areas stained with NeuN or DAPI were calculated using ImageJ (NIH). The data are presented as a ratio of the integrated densities of NeuN to those of DAPI. For comprehensive measurement along the long axis of the hippocampus, we analyzed the septal, medial, and temporal sections of the hippocampus alongside the dorsal and ventral DG in each section.

### Behavioral tests

The behavioral tests were conducted in a dimly lit behavioral room during the dark phase of the day cycle. All mice were habituated in the behavioral room for 1 h prior to testing. To minimize unnecessary stress during testing, all of the mice were handled daily, and the testing apparatus and arenas were cleaned with 70% ethanol and dried after each mouse was tested.

#### *Y-maze forced alteration test*

The Y-maze test was conducted in a Y-shaped plastic maze (34 cm × 6 cm × 10 cm) that had three identical arms (start, familiar, and novel/closed), as described previously (Dinel et al., 2014). The test consisted of video-recorded acquisition and retrieval trials separated by 30-min inter-trial intervals. During the acquisition trial, one arm was closed with a door, and a mouse was placed in an open-arm (start) end and allowed to explore the two open arms for 5 min. After 0.5 h, the retrieval trial was performed by removing the door from the closed arm (novel) and allowing the mouse to freely explore all of the arms (start, familiar and novel) for 5 min. The start and novel arms were randomized for each mouse to minimize side bias. The frequency of entries and the latency to first entry into the novel and familiar arms were analyzed using ANY-maze software (ANY-maze, IL, USA).

#### *Object recognition test*

The object recognition test consisted of two sessions: acquisition and retrieval. During the 5-min acquisition phase, each mouse was allowed to explore two identical objects at each of the two opposite corners of an open field arena (40 cm × 40 cm × 40 cm). During the 5-min retrieval phase, the mouse was allowed to encounter 2 objects after a 90-min delay: a familiar object to which the mouse had already been exposed and a new object. The total distance traveled and the interaction time (s) with the novel object were measured and analyzed from the recorded video using video tracking software (ANY-maze). Preference index of novel object recognition was calculated by [(novel object exploration time)/(total objects exploration time)] × 100.

#### *Open-field test*

The open-field test was performed as previously described, with minor modifications (Lim et al., 2016). In brief, each mouse was placed in the middle of an enclosed white plastic box (40 cm × 40 cm × 40 cm) and allowed to explore the box for 10 min. Each trial was video recorded, and the distance traveled and time spent in the center or outer areas were measured and analyzed using ANY-maze.

#### *Novelty-suppressed feeding test*

This test was conducted as previously described, with minor modifications (Yalcin et al., 2011). Briefly, food and water bottles were removed from the home cage 24 h before testing. During the test, regular chow pellets were placed on a petri dish in the center of an open field box (40 cm × 40 cm × 40 cm) illuminated under a 450-lux light. The mouse was placed in a corner of the open field, and the latency to feed (biting) was video recorded for 5 min and recorded using a stopwatch.

## QUANTIFICATION AND STATISTICAL ANALYSIS

All data are expressed as means ± standard deviations (SD) of the mean and analyzed using SPSS v25 statistical analysis software. Graphs were plotted using Prism software v8.02 (GraphPad Software Inc). Statistical significance was determined using analysis of variance (ANOVA) between groups and paired *t* tests within a group unless otherwise stated (*$p < 0.05$; **$p < 0.01$; n.s: not significant).